photonics

MDPI

Article

Enhancing Dynamic Performance in K-Rb-^{21}Ne Co-Magnetometers through Atomic Density Optimization

Lv Yang [1], Haoying Pang [1,2,*] and Wei Quan [1,2]

[1] School of Instrumentation and Optoelectronic Engineering, Beihang University, Beijing 100191, China; 452739219@buaa.edu.cn (L.Y.); quanwei@buaa.edu.cn (W.Q.)
[2] Institute of Large-Scale Scientific Facility and Centre for Zero Magnetic Field Science, Beihang University, Beijing 100191, China
* Correspondence: panghaoying@buaa.edu.cn

Abstract: The K-Rb-^{21}Ne co-magnetometer exhibits poorer dynamic performance due to the larger equivalent magnetic field generated by alkali metal atoms. In this study, the impact of the atomic number density of alkali metal atoms and noble gas atoms in the cell on the dynamic performance of the atomic ensemble is investigated quantitatively. Relationships between the slow-decay term in the transient response attenuation of the Spin-Exchange Relaxation-Free (SERF) co-magnetometer to interference magnetic fields and the number densities of noble gas atoms as well as alkali metal atoms are established. Based on the established model, the relationship between the number density of ^{21}Ne atoms and dynamic performance is investigated using cells with five different noble gas pressures. Then, we investigate the impact of the number density of alkali metal atoms using a cell with a pressure of 2.1 atm at different temperatures. The results indicate that, as the number density of alkali metal atoms or noble gas atoms in the cell increases, the dynamic performance of the system improves, which provides a theoretical basis for the design of cell parameters for SERF co-magnetometers.

Keywords: SERF co-magnetometer; atomic number density; dynamic performance; atomic cell

Citation: Yang, L.; Pang, H.; Quan, W. Enhancing Dynamic Performance in K-Rb-^{21}Ne Co-Magnetometers through Atomic Density Optimization. *Photonics* **2024**, *11*, 182. https://doi.org/10.3390/photonics11020182

Received: 20 January 2024
Revised: 8 February 2024
Accepted: 13 February 2024
Published: 16 February 2024

1. Introduction

Ultra-sensitive co-magnetometers use alkali metal and noble gas spin species to simultaneously and accurately measure rotation [1], and have been used in a variety of applications, including rotation sensing [2–4], biomagnetism [5], and fundamental physics such as testing for CPT symmetry [6,7], the Electron Dipole Moment [8], and spin-depended forces [9,10]. In recent years, atomic spin co-magnetometers based on Spin-Exchange Relaxation-Free (SERF) principles have become a significant development direction in inertial instrumentation [11–13]. Due to its inherent advantages of high precision and compact size, the SERF co-magnetometer is well-suited for prolonged, high-precision inertial navigation applications [14,15]. When the atomic ensemble is in a low magnetic field with high atomic density, the spin-exchange relaxation between electron spins is significantly reduced, which leads to an increase in coherent time and an improvement in measurement sensitivity. During the process of measuring inertial signals, the electron spin is in the SERF regime, enabling the detection of nuclear spin precession induced by the inertial measurement torque.

In 2005, a co-magnetometer based on K-^{3}He, demonstrated by the Romalis group, achieved a rotation sensitivity of 5×10^{-7} rad/s/Hz$^{1/2}$ [16]. Subsequently, co-magnetometers utilizing atomic sources such as Cs-^{129}Xe, Rb-^{129}Xe have been employed for inertial measurements [17,18]. In the selection of atomic sources, the technique of hybrid pumping with at least two alkali metal atoms is applied to achieve better polarization uniformity [19]. On the other hand, due to the fact that the gyromagnetic ratio of ^{21}Ne is smaller than that of other noble gas atoms such as ^{3}He and ^{129}Xe, it possesses a higher ultimate sensitivity.

Therefore, co-magnetometers based on K-Rb-^{21}Ne are a primary research direction in SERF inertial measurements currently [20].

However, the dynamic performance of the K-Rb-^{21}Ne SERF co-magnetometer is comparatively inferior to other atomic source combinations due to the significant contribution of the equivalent magnetic field generated by electrons [21]. Therefore, after determining the atomic source, optimization of cell parameters and operating conditions is necessary. The magnitude of the equivalent magnetic field generated by electron and nuclear spin polarization depends on their respective atomic number densities. During chamber pressurization, the pressure of the injected gas determines the number density of noble gas atoms, while the cell temperature at the steady-state operating point of the system determines the number density of alkali metal atoms.

This paper primarily investigates the impact of the number density of noble gas and alkali metal atoms inside the cell on the dynamic performance of nuclear spin self-compensation in the K-Rb-^{21}Ne ensemble. We systematically investigated the transient response process of the K-Rb-^{21}Ne co-magnetometer and analyzed the relationship between the decay term of nuclear spin precession in the transient response and the atomic number density of noble gas atoms as well as alkali metal atoms. Based on the aforementioned research, we conducted theoretical simulations to investigate the influence of noble gas pressure and cell temperature on the characteristic time of the transient response in our system. Subsequently, we designed experiments to validate these findings. We measured the transient responses of cells with different pressures at the same cell temperature and assessed the dynamic performance of the same cell at different temperatures.

2. Theory

2.1. Basic Principle

The spin-exchange relaxation-free co-magnetometer with hybrid pumping involves the concurrent utilization of two alkali metal atoms, K and Rb, in conjunction with the noble gas Ne atoms. The proportion of K and Rb atoms typically falls within the range of 1:80 to 1:300 [22]. Circularly polarized light is employed to optically situate K atoms on the D1 line, with subsequent polarization transfer occurring via spin-exchange collisions with Rb atoms.

Subsequently, alkali metal atoms, through further spin-exchange collisions, induce hyperpolarization in ^{21}Ne atoms. Ultimately, the transverse polarization of alkali metal atoms is obtained by employing linearly polarized light on the D1 line of Rb atoms. To induce the atomic ensemble into the SERF regime, it is imperative to satisfy two criteria: a high atomic density and a low external magnetic field. To fulfill these prerequisites, the alkali metal cell is situated within a magnetic shielding system and heated to a temperature range of 160 to 200 °C. Under this condition, the atomic number density of Rb reaches approximately $10^{14} \sim 10^{15}$ cm^{-3} [23,24]. Consequently, the spin-exchange relaxation between alkali metal atoms dominates over other interactions. Hence, treating both alkali metal species as equivalent becomes a justifiable simplification.

In the SERF atomic spin inertial measurements, there exists a strong coupling between electron and nuclear spins. When the Larmor precession frequency of the electron spin is approximately equal to that of the nuclear spin, the nuclear spin experiences rapid decay due to the influence of the electron spin. This leads to the system swiftly reaching a steady state. The evolution of the spin polarization of alkali metal atoms $\mathbf{P}^e$ and the nuclear spin polarization of noble gas atoms $\mathbf{P}^n$ over time is described by the following expressions [16]:

$$\begin{aligned}\frac{\partial \mathbf{P}^e}{\partial t} =& \frac{\gamma_e}{Q}(\mathbf{B} + \lambda M^n \mathbf{P}^n + \mathbf{L}) \times \mathbf{P}^e - \mathbf{\Omega} \times \mathbf{P}^e \\ &+ \frac{1}{Q}\left(R_p \mathbf{s}_p + R_m \mathbf{s}_m + R_{se}^{en} \mathbf{P}^n\right) - \frac{1}{Q}\{R_2^e, R_2^e, R_1^e\}\mathbf{P}^e \\ \frac{\partial \mathbf{P}^n}{\partial t} =& \gamma_n(\mathbf{B} + \lambda M^e \mathbf{P}^e) \times \mathbf{P}^n - \mathbf{\Omega} \times \mathbf{P}^n + R_{se}^{ne} \mathbf{P}^e \\ &- \{R_2^n, R_2^n, R_1^n\}\mathbf{P}^n\end{aligned} \tag{1}$$

The right-hand side of the equation can be divided into three components. The first component represents the Larmor precession term due to the interaction between atomic spin and the magnetic field. The second component corresponds to the effective precession term caused by the rotation relative to the inertial frame. The third component accounts for the exchange collisions and relaxation terms among atoms within the system. Here, γ_e and γ_n represent the gyromagnetic ratios of electrons and noble gas atoms, respectively. Q is the slowing-down factor, characterizing the Larmor precession slowdown due to spin-exchange collisions. The magnetic field-related term **B** denotes the external magnetic field, while $\lambda M^n \mathbf{P}^n$ and $\lambda M^e \mathbf{P}^e$ are the equivalent magnetic field terms for interactions between alkali metal atoms and noble gas atoms. Here, λ stands for the Fermi contact interaction enhancement factor, and M^e and M^n are the magnetic moments when the electron spin and nuclear spin are fully polarized, respectively. **L** is the light-shift generated by the AC Stark effect. $\mathbf{\Omega}$ is the input angular velocity, also serving as the measured quantity in the co-magnetometer. In the third section, R_p and R_m denote the pumping rates of the pump light and the probe light, respectively. These rates are primarily associated with the power density and frequency selected for the lasers. The vectors s_p and s_m characterize the circular polarization and propagation direction of the pump and probe lasers. R_{se}^{en} and R_{se}^{ne} represent the spin-exchange collision relaxation terms between alkali metal electron spin and noble gas nuclear spin. R_1^e and R_2^e correspond to the longitudinal and transverse relaxation rates of electron spin. Similarly, R_1^n and R_2^n denote the longitudinal and transverse relaxation rates of noble gas nuclear spin.

We express the transverse component of the polarization intensity as $P_\perp^e = P_x^e + iP_y^e$, $P_\perp^n = P_x^n + iP_y^n$. Also, the transverse components of the input magnetic field term and the inertial signal are denoted as $B_\perp = B_x + iB_y$, $\Omega_\perp = \Omega_x + i\Omega_y$ respectively. Consequently, we represent Equaion (1) in the following form:

$$\begin{bmatrix} \frac{\partial P_\perp^e}{\partial t} \\ \frac{\partial P_\perp^n}{\partial t} \end{bmatrix} = \begin{bmatrix} i\omega_e - \frac{R_2^e}{Q} & \frac{R_{se}^{ne}}{Q} - i\omega_{en} \\ R_{se}^{en} - i\omega_{ne} & i\omega_n - R_2^n \end{bmatrix} \begin{bmatrix} P_\perp^e \\ P_\perp^n \end{bmatrix} + \begin{bmatrix} b_x^e + ib_y^e \\ b_x^n + ib_y^n \end{bmatrix} \tag{2}$$

where

$$\begin{aligned}\omega_e =& \frac{\gamma_e}{Q}(B_z + L_z + \lambda M_0^n P_z^n) - \Omega_z, \omega_{en} = \frac{\gamma_e}{Q}\lambda M_0^n P_z^e \\ \omega_n =& \gamma_n(B_z + \lambda M_0^e P_z^e) - \Omega_z, \omega_{ne} = \gamma_n \lambda M_0^e P_z^n \\ b_x^e =& P_z^e\left(\frac{\gamma_e}{Q}B_y - \Omega_y\right), b_y^e = -P_z^e\left(\frac{\gamma_e}{Q}B_x - \Omega_x\right) \\ b_x^n =& P_z^n(\gamma_n B_y - \Omega_y), b_y^n = P_z^n(\gamma_n B_x - \Omega_x)\end{aligned} \tag{3}$$

As illustrated in Figure 1, if the system experiences a step-wise transverse magnetic field disturbance under steady-state conditions, exemplified by applying a step-wise magnetic field B_y along the y-axis, the information from the electron spin is transformed into an output electrical signal through the detection system [25]. We can observe oscillations in the output signal, reaching a new steady state. In the figure, B_z represents the externally ap-

plied main magnetic field through the coil, while B_e and B_n denote the equivalent magnetic fields generated by alkali metal atoms and noble gas atoms, respectively:

$$\begin{aligned}\mathbf{B_e} &= \lambda M_0^e \mathbf{P^e} = \frac{2}{3}\kappa\mu_0\mu_B n_e \mathbf{P^e} \\ \mathbf{B_n} &= \lambda M_0^n \mathbf{P^n} = \frac{2}{3}\kappa\mu_0\mu_N n_n \mathbf{P^n}\end{aligned} \tag{4}$$

where κ represents the Fermi contact constant for the Rb-Ne pair. μ_0 is the Bohr magneton, and μ_N is the nuclear spin magnetic moment. n_e and n_n denote the densities of Rb atoms and ^{21}Ne atoms, respectively. The transverse polarization of the electron can be described by the following expression:

$$\begin{aligned}P_x^e(t) &= P_0 + \mathrm{Re}[P_\perp^e(t)] \\ &= P_0 + \sum_j^{e,n} P_0^j e^{-\lambda_{jr}t}\cos(\lambda_{ji}t + \Phi_j)\end{aligned} \tag{5}$$

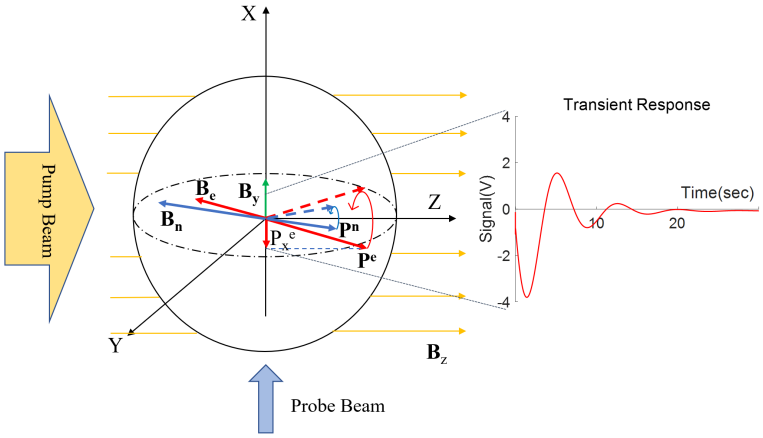

Figure 1. The schematic of the transient response process.

$P_x^e(t)$ can be divided into three components: the steady-state term, the rapidly varying term characterizing the electron oscillations, and the slowly varying term characterizing the nuclear oscillations. Here, P_0 is the polarization of the electron in the x-direction at steady state, and P_{0e} and P_{0n} represent the polarization of the initial signal. λ_{er} and λ_{ei}, respectively, characterize of the characteristic time and the characteristic frequency of alkali metal electron precession. Similarly, λ_{nr} and λ_{ni}, respectively, characterize the characteristic time and the characteristic frequency of noble gas nuclear precession. Φ_e and Φ_n are random initial phases. The expressions for each characteristic value are as follows:

$$\begin{aligned}\lambda_{er} &= -\frac{R_2^e/Q + R_2^n}{2} + \frac{1}{2\sqrt{2}}\sqrt{\sqrt{a^2+b^2}+a} \\ \lambda_{ei} &= \frac{1}{2}(\omega_e+\omega_n) + \frac{1}{2\sqrt{2}}\mathrm{Sign}[b]\sqrt{\sqrt{a^2+b^2}-a} \\ \lambda_{nr} &= \frac{R_2^e/Q + R_2^n}{2} - \frac{1}{2\sqrt{2}}\sqrt{\sqrt{a^2+b^2}+a} \\ \lambda_{ni} &= \frac{1}{2}(\omega_e+\omega_n) - \frac{1}{2\sqrt{2}}\mathrm{Sign}[b]\sqrt{\sqrt{a^2+b^2}-a}\end{aligned} \tag{6}$$

where

$$\begin{aligned}a &= (R_2^e/Q - R_2^n)^2 - (w_e - w_n)^2 + 4R_{se}^{ne}R_{se}^{en}/Q - 4\omega_{ne}\omega_{en} \\ b &= -2(R_2^e/Q - R_2^n)(w_e - w_n) - 4(R_{se}^{ne}\omega_{ne}/Q + R_{se}^{en}w_{en})\end{aligned} \tag{7}$$

Due to the significantly greater relaxation rate of Rb atoms compared to ^{21}Ne atoms, the rapidly varying part of the characteristic roots in Equation (4) has a duration in the oscillating signal of less than 0.05 s, making it difficult to observe. This has a relatively minor impact on the indicators for long-duration inertial measurements. Therefore, in this paper, our primary focus is on the slowly varying term λ_{nr}, which is more readily observable. When the system operates under different main magnetic fields, the characteristic time of the transient response varies. The dynamic performance of the system's nuclear spin self-compensation can be characterized using the slow-decay term. In environments where magnetic field disturbances are frequent, a larger λ_{nr} value will also reduce the impact of overshooting on long-term stability. The system exhibits optimal dynamic performance when λ_{nr} reaches its maximum. Setting $d\lambda_{nr}/dB_z = 0$ allows us to obtain:

$$B_{zf} = \frac{-B_z^n\gamma_e + B_z^e\gamma_n Q}{\gamma_e(1 - Q\gamma_n/\gamma_e)} \tag{8}$$

At this point, the precession frequencies of electron and nuclear spins are equal, and the system exhibits the fastest precession frequency and the highest relaxation rate, resulting in optimal dynamic performance. However, at this point, the system cannot fully compensate for external interfering magnetic fields, and its sensitivity to inertial signals decreases. Typically, to enhance the nuclear spin self-compensation capability of the system, the operational point is positioned at the magnetic compensation point $B_c = -\lambda M_0^n P_z^n - \lambda M_0^e P_0^e - B_{za}$, where B_{za} represents the residual magnetization magnitude in the environment. Under the influence of transverse magnetic field disturbances, when the system operates with the magnetic field set at $B_z = B_c$, the signal bias remains unchanged when the system eventually returns to its steady-state value. Hence, in addition to the point of fastest response, this paper primarily focuses on the dynamic performance of the system at $B_z = B_c$.

2.2. Simulation

For ease of experimental validation, we simulate and analyze the variation patterns of the slowly varying term λ_{nr} of the system's characteristic roots with changes in noble gas pressure and cell temperature.The parameter values used in the simulation are presented in Table 1.

Table 1. Variables used for simulations.

Parameter	Value
Gyromagnetic ratio of the electron spin γ_e	$2\pi \times 28$ Hz/nT
Gyromagnetic ratio of the electron spin γ_n	$2\pi \times 0.00336$ Hz/nT
Fermi contact enhancement factor between Rb and ^{21}Ne atoms κ	35.7 ± 3.7 [26]
Permeability of vacuum μ_0	$4\pi \times 10^{-7}$ N/A^2
Bohr magneton μ_B	9.274×10^{-24} J/T
Nuclear spin magnetic moment μ_N	3.343×10^{-27} J/T [27]
Number density of Rb atoms n_e at 180 °C	4.04×10^{14} cm^{-3}
Transverse relaxation rate of electron spin at 180 °C	1466.51 1/s

The impact of the noble gas pressure on λ_{nr} is analyzed. As shown in Figure 2 below, the curve represents the variation in λ_{nr} with p_n at a temperature of 180 °C. The noble gas pressure p_n primarily determines the value of the nuclear equivalent magnetic field B_n by influencing the ^{21}Ne atomic number density n_n and the nuclear spin relaxation term R_1^n. The following relationship between noble gas pressure and the atomic number density exists at charging temperature of $T_0 = 298.15$ K:

$$n_n = \frac{p_0 p_n N_A}{RT_0} \tag{9}$$

where $p_0 = 101{,}325$ Pa is the standard atmospheric pressure. N_A denotes the Avogadro's constant, and R represents the molar gas constant. The longitudinal relaxation rate of nuclear spin is $R_1^n = R_{se}^{ne} + R_{quad} + R_{\nabla B}$. Here, R_{quad} is the relaxation due to the electric quadrupole moment interaction between ^{21}Ne and the cell wall, and $R_{\nabla B}$ denotes the relaxation due to the longitudinal magnetic field gradient, both of which are influenced by p_n. The relationship between p_n and B_n can be expressed in the following form [28]:

$$B_n = \frac{2}{3}\kappa\mu_0\mu_N n_n(p_n)\frac{R_p}{R_1^n(p_n)} \tag{10}$$

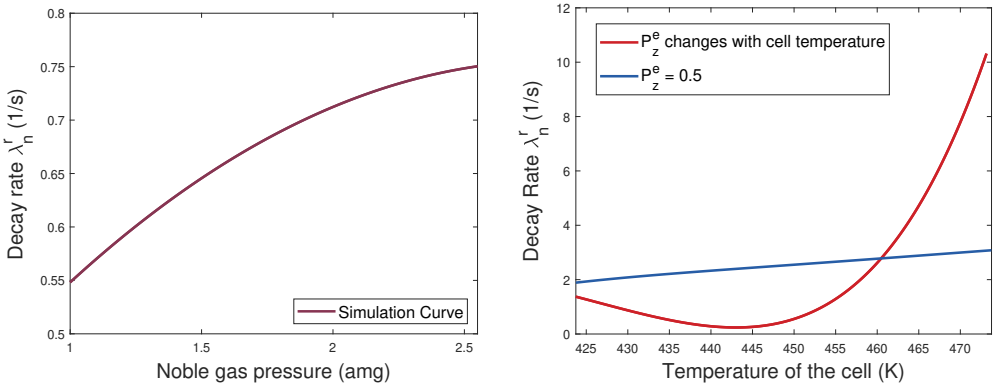

(**a**) (**b**)

Figure 2. (**a**) Simulation curve of the nuclear decay rate λ_{nr} varying with the noble gas pressure at 180 °C. (**b**) Simulation curve of the nuclear decay rate λ_{nr} varying with the cell temperature for a 2.1 atm cell.

The above equation is implicit; therefore, in the simulation, the positive pressure part of this relationship is approximated using a polynomial. Given that R_2^e is theoretically almost unaffected by inert gas pressure, the value of B_n plays a decisive role in determining λ_{nr}. As depicted in Figure 2a, both exhibit a similar trend, with p_n, indicating that as noble gas pressure increases, the decay of nuclear spin oscillations accelerates, albeit at a reduced rate of change.

For a cell with a ^{21}Ne pressure of 2.1 atm, the dynamic performance of the system varies at different temperatures. The temperature primarily influences various indicators of the entire atomic ensemble by determining the atomic number density of Rb atoms. Additionally, temperature changes can cause variations in the diffusion coefficients and the average relative velocity of atoms within the system, but these effects are nearly negligible compared to the changes in n_{Rb}. In the cell described in this paper, the density of Rb atoms can be obtained using the saturated vapor pressure formula:

$$n_{Rb} = \frac{1}{T}10^{21.866+A-B/T} \tag{11}$$

where $A = 4.312$, $B = 4040$ are alkali number density constants of Rubidium. When the temperature changes, the electron polarization P_z^e also varies. In this case, by adjusting the optical power density of the pump light, P_z^e can be maintained at 0.5 to achieve the maximum measurement sensitivity. As shown in Figure 2b, when P_z^e is kept constant, the final value of λ_{nr} increases with temperature due to the higher number density of Rb atoms. Without changing the optical power density of the pump light, P_z^e decreases with increasing temperature as the relaxation rate R_1^e increases. However, the impact of the increase in atomic number density outweighs the decrease in P_z^e, resulting in an increase in the electron polarization magnetic field B_e with temperature elevation. Generally, at lower temperatures, the dominant effect on dynamic performance is the decrease in electron polarization as the temperature rises, leading to a decrease in λ_{nr}. After reaching a certain

extremum, the increased transverse relaxation of electrons becomes dominant, causing λ_{nr} to rapidly increase with rising temperature. The extremum point varies with the selected pump light power.

3. Experimental Results and Discussion

3.1. Experimental Setup

To validate the above analytical results, an experimental setup is constructed as shown in Figure 3. A circularly polarized 30 mW pump light of the K D1 line is used to polarize K atoms, passing through the cell along the z-axis after being collimated by two lenses. The transverse polarization of electrons P_x^e is detected by a linearly polarized 580 µW probe laser with a red-detuned frequency of 0.3 nm from the Rb D1 line.

The power of the pump and probe light is controlled by a stable intensity system consisting of a liquid crystal delay. A 10 mm spherical cell is installed in a boron nitride oven heated by a 110 kHz AC power. To maintain polarization uniformity, the content of K in the alkali metal mixture is kept low. Additionally, 20 Torr nitrogen gas is introduced into the cell as a quenching gas to suppress electron spin radiation capture. The magnetic shielding system consists of active magnetic compensation and passive magnetic shielding. The outer layer of the oven is equipped with three-axis magnetic field coils used to generate uniform fields. For passive magnetic shielding, the system employs a structure consisting of two layers of μ-metal and one layer of MnZn–ferrite to reduce external magnetic field interference and minimize magnetic noise.

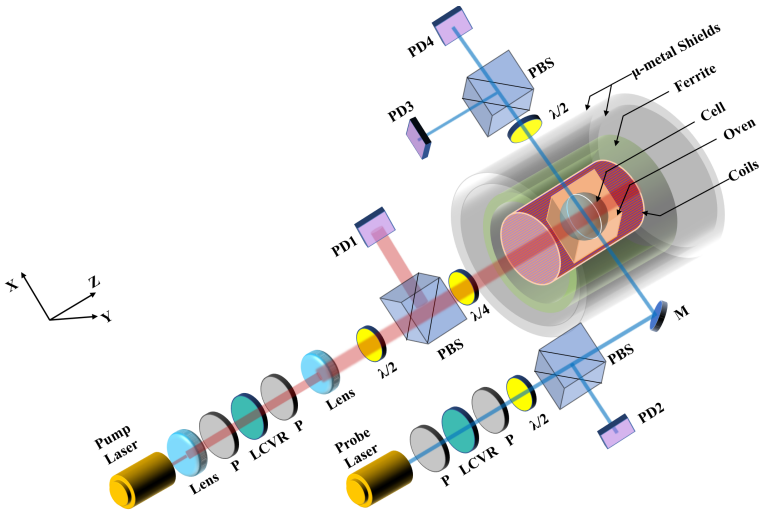

Figure 3. The experimental setup of hybrid optically pumped SERF co-magnetometer. Heater: AC current-driven heating system to heat the cell; active magnetic field compensation: magnetic coils; passive magnetic field shielding: μ-metal shields and ferrite magnetic shield; P: linear polarizer; $\lambda/2$: half wave plate; $\lambda/4$: quarter wave plate; LCVR: liquid crystal variable retarder; PBS: polarizing beam splitter; PD: photodiode; M: reflection mirror.

3.2. Results and Discussion

Figure 4 illustrates the transient response process of the system. When the system is in a steady state, the magnitude of the z-axis main magnetic field is 192.5 nT. At this point, a step magnetic field of around 1 nT is applied in the y-axis direction using a signal generator, and the response signal is acquired using NI-4431 with a sampling rate of 2 kHz. The signal exhibits two oscillation processes, with the response of the electron spin almost returning to steady state within 0.02 s, while the slower response of the nuclear spin takes more than 10 s to stop oscillating. The parameters determining the oscillation decay rates are λ_{er} and λ_{nr}. After determining the start and end time of oscillations based on the signal, electron and nuclear spin oscillations are divided and parameter fitting is conducted. During the fitting progress, adjusting the upper and lower bounds of parameter λ_{nr} allows us to

achieve the target values of characteristic times and frequencies. According to Equation (6), $\lambda_{er} + \lambda_{nr} = R_2^n/2$. The faster the decay of electron spin oscillations, the slower the decay of nuclear spin oscillations. Under the same step magnetic field applied with different main magnetic fields B_z, characteristic times and frequencies of signal oscillations at different operating points can be obtained.

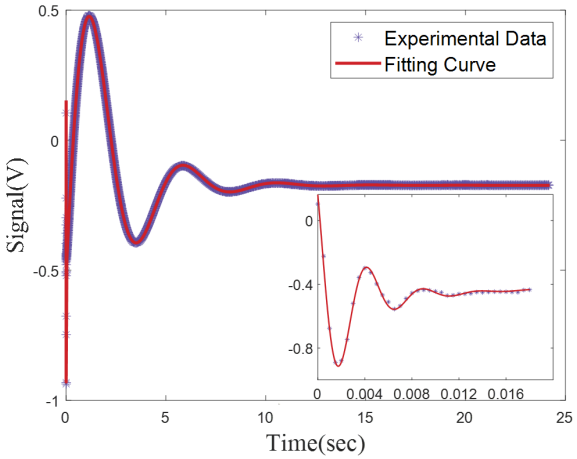

Figure 4. The transient response of the SERF co-magnetometer consisting a faster oscillation of the electron spin and a slower oscillation of the nuclear spin.

An experiment was conducted with a cell containing ^{21}Ne at a pressure of 2.1 atm at 180 °C. After hyperpolarization, the compensation point B_c of the system is 171.7 nT. By varying the value of the main magnetic field B_z and applying the same step magnetic field of around 1 nT, oscillation curves were obtained. For each oscillation curve, fitting using Equation (5) provided the reciprocal of the characteristic time (λ_{nr}) and the characteristic frequency (λ_{ni}) of the transient response of noble gas atoms. By fitting the obtained data points using Equation (6), the curve in Figure 5 was obtained. When $B_{zf} = 126.1$ nT, there is strong coupling between alkali metal atoms and noble gas atoms. At this point, the precession frequencies of both are nearly equal, resulting in the fastest overall precession decay rate and optimal dynamic performance. At the compensation point B_c, the precession frequency and relaxation rate significantly decrease compared to B_{zf}.

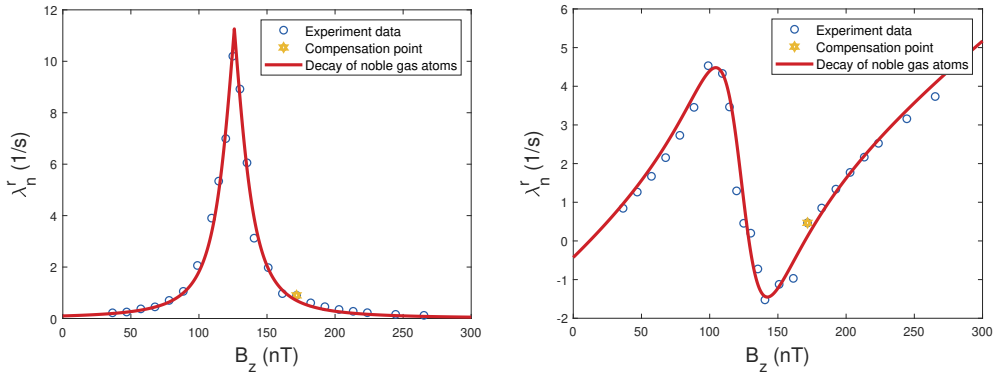

Figure 5. Decay rates and precession frequencies of the transient responses of the nuclear spins as a function of the main magnetic field B_z. (**a**) Decay rates of the nuclear spins λ_{nr}. (**b**) Precession frequencies of the nuclear spins λ_{ni}.

The precession frequencies between alkali metal atoms and inert gas atomic nuclei become mismatched, leading to a reduction in dynamic performance. When B_z is very far from B_{zf} ($|B_z| \to \infty$), the time for oscillation decay back to steady state tends

toward the relaxation time of ^{21}Ne. At this point, electron spin and nuclear spin are completely decoupled.

Next, the relationship between atomic number density and the dynamic performance of the system is investigated. The pressure of the introduced noble gas determines the atomic number density of the ^{21}Ne atoms. Five 10 mm spherical cells with alkali metal densities close to each other and ^{21}Ne pressures of 0.7 atm, 1.1 atm, 1.4 atm, 2.1 atm, and 2.4 atm, respectively, are used for transient response testing. The differences in density ratios among the five cells result in variations in the transverse relaxation of nuclear spins. However, compared to electron spin relaxation R_2^e, the impact on dynamic performance is practically negligible. Figure 6a presents the decay rates for each cells at different main magnetic fields, where the x-axis is $\delta B_z = B_z - B_c$. The values of λ_{nr} at the compensation point for the five cells are 0.3314 1/s, 0.7015 1/s, 0.8995 1/s, 1.267 1/s, and 1.302 1/s. Due to the presence of the equivalent magnetic field generated by alkali metal electrons and the residual magnetization inside the shielding cylinder, the points with the fastest response are all located below the compensation point. The optimal operating point for dynamic performance is $B_{zf} \approx -B_n$, so the difference between this point and the compensation point yields the magnitude of the combined magnetic field between the residual magnetic field B_{za} and the electron magnetic field B_e. The impact of varying the noble gas pressure in the cell on B_e is relatively minor. The experiment is conducted swiftly to minimize the impact of slow-changing external conditions. The discrepancies in residual magnetism primarily stem from installation errors introduced during the replacement of the cell. Consequently, the figure can reflect the residual magnetism within the shielding cylinder after each cell replacement-induced demagnetization.

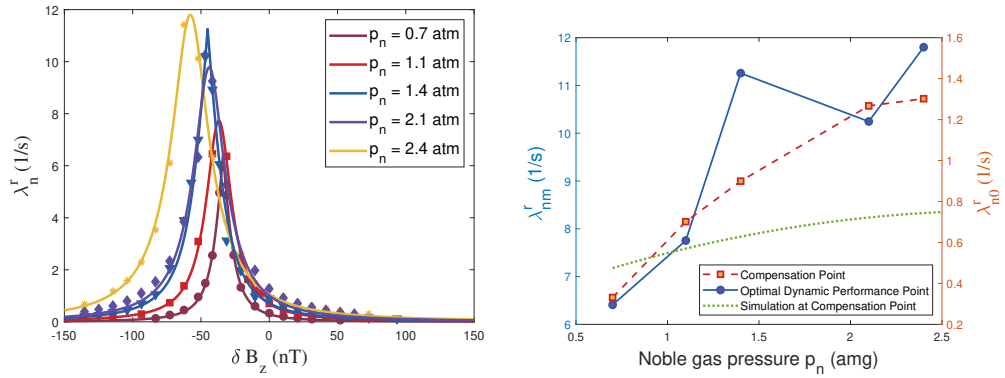

(**a**) (**b**)

Figure 6. (**a**) The nuclear spin slow−decay rate λ_{nr} as a function of deviation from the compensation point δB_z utilizing cells of different noble gas pressure. (**b**) The changing law of λ_{nr} under different p_n.

For ease of comparison, Figure 6b provides the decay rates of nuclear magnetic fields at both the compensation point (indicated by the red dashed line on the right vertical axis) and the point of fastest response (represented by the blue solid line on the left vertical axis) for different noble gas pressures. Similar to the previous simulation result (depicted by the green dotted line in the figure), as the pressure of noble gas increases, the dynamic performance of the system improves. However, there is a certain deviation in the specific numerical values compared to the simulation result. This discrepancy arises from the differences in R_2^e and the transverse residual magnetic field gradient between the simulation and experiments. In the experimental process, it is necessary to disassemble the shield tube to replace the cell, inevitably resulting in errors in these two parameters. Concerning the point of fastest response, the overall dynamic performance increases with the growth of gas pressure, except for the chamber with p_n = 1.4 atm, indicating the need for further validation.

The cell temperature governs the number density of Rb atoms. Tests were conducted on the cell with a ^{21}Ne pressure of 2.1 atm at temperatures of 170 °C (443.15 K), 175 °C,

180 °C, 185 °C, and 190 °C (463.15 K), respectively. Maintaining a constant electron polarization requires optimizing the pumping light power for each temperature point. However, optimizing the pumping light power for each temperature point elongates the experimental cycle, as measuring the intensity of electron polarization disrupts initial operating state, thereby amplifying the impact of environmental changes. The experimental test data for this study involved only variations in cell temperature. The relationship between decay rates and δB_z at different temperature points is illustrated in Figure 7a. From 170 °C to 190 °C at these five temperature points, the values of λ_{nr} at the compensation point are 0.3083 1/s, 0.8812 1/s, 1.267 1/s, 2.259 1/s, and 3.429 1/s, respectively. When altering only the temperature without replacing the cell, the ambient residual magnetization B_{za} remains almost constant. The primary variation between the fastest response point and the compensation point is attributed to the change in B_e. With increasing temperature, the polarization intensity of electrons diminishes, but the electron density increases, ultimately leading to an augmentation in the equivalent magnetic field of electrons B_e. In Figure 7b, the red dashed line represents the decay rate at the compensation point, gradually increasing with temperature. The green dotted line in the figure corresponds to the previous simulation results, exhibiting an overall trend consistent with the experimental measurements. The discrepancy between the red line and the green line primarily arises from two sources. In the simulation calculations, the alkali metal atom density is computed based on Equaion (11), which is an empirical formula with typically up to 15% of error. Also, when calculating the electron spin magnetic field magnitude, the Fermi contact constant used introduces approximately 10% of error.

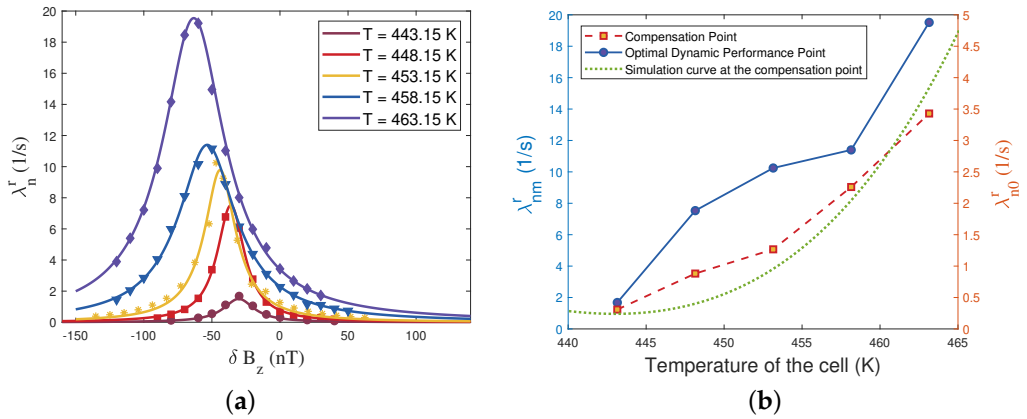

(**a**) (**b**)

Figure 7. (**a**) The nuclear spin slow-decay rateλ_{nr} as a function of deviation from the compensation point δB_z at different cell temperatures. (**b**) The changing law of λ_{nr} under different cell temperatures.

The pressure data in the cell may exhibit variability due to the need for cell replacement, leading to multiple variables and potentially poor quantitative data repeatability (as seen in the difference between the simulated and actual measurement results in the graph). However, under conditions where experimental parameters are kept as consistent as possible, the pattern of the nuclear spin oscillation decay rate with pressure variation should remain consistent. In experiments involving cell temperature, there are fewer changes in external conditions compared to the previous experiment. In the short term, data repeatability can be achieved fairly well. However, over time, the influence of environmental temperature on external optical components and mechanical vibrations can affect the stability of the system to some extent.

From the preceding results, it can be inferred that increasing ^{21}Ne pressure enhances the dynamic performance of the atomic ensemble at the compensation point. However, due to constraints imposed by cell manufacturing technology and the material strength of cell glass, the pressure cannot be increased indefinitely. In general, for neon gas with a ^{21}Ne abundance of 70%, surpassing 3.5 atm necessitates using liquid helium cooling instead of liquid nitrogen cooling. Present technology does not support the fabrication of cells

exceeding 12 atm [29]. High-pressure cells also impose requirements on the thickness of the cell walls. Excessive thickness of the walls would result in an increase in the divergence angle of parallel light passing through the spherical cell. Additionally, while increasing pressure, it concurrently diminishes the effectiveness of the nuclear spin self-compensation, thereby reducing its sensitivity in inertial measurements [28]. When increasing the cell temperature, maintaining a constant electron polarization of 0.5 requires an increase in the pumping light power density. However, when utilized in devices such as compact gyroscopes, the power of the pumping laser is constrained. Achieving the previous value of electron polarization becomes challenging when the cell temperature exceeds 195 °C. On the other hand, without adjusting the pumping light power, the sensitivity coefficient of the output signal to temperature will change, thereby impacting the sensitivity of inertial measurements [30]. As a consequence, when determining the cell pressure and the operating temperature of the cell, a trade-off must be made between the dynamic performance of the system and the sensitivity of inertial measurements.

For other types of atomic ensembles, their dynamic performance differs from the K-Rb-^{21}Ne ensemble. In the case of the ^{129}Xe ensemble, at the same total pressure, due to the gyromagnetic ratio of ^{129}Xe atoms being three times larger than that of ^{21}Ne, the magnetic field is 10 times that of the Ne ensemble, resulting in the fastest decay rate. Conversely, the ^{3}He ensemble, at the same noble gas pressure, exhibits the smallest electron relaxation rate and the smallest magnetic field produced by the electron spin–nuclear spin coupling ensemble. Therefore, it has the lowest decay rate. However, due to its small electron magnetic field, its contribution is minimal, and the compensation point is close to the fastest response point, especially at high pressures.

4. Conclusions

In conclusion, we investigated the influence of the atomic number density of alkali metal atoms and noble gas atoms in the cell on the dynamic performance of the K-Rb-^{21}Ne hybrid pumped co-magnetometer. By analyzing the transient response of the system to transverse magnetic field disturbances, the relationship between the slow-decay term in the transient response and various magnetic field terms, as well as relaxation terms in the system was obtained. Subsequently, the relationship with atomic number density was established. The atomic number density of ^{21}Ne atoms in the cell is determined by the pressure of the noble gas during cell pressurization, while the atomic number density of Rb atoms is determined by the cell temperature during the operation. We selected cells with five different pressures and measured their transient responses to a step magnetic field in the y-direction. By fitting parameters, we obtained the nuclear spin decay rates. Simultaneously, we conducted tests at five temperature points in a 2.1 atm cell. Experimental results indicate that as the density of noble gas and alkali metal atoms increases, the dynamic performance of the system improves. However, this is in contradiction with the sensitivity of the inertial measurements, necessitating a trade-off based on practical requirements. This paper enhances the dynamic performance of the SERF atomic co-magnetometer by optimizing the atomic number density within the cell. It provides a theoretical basis for the parameter design of cells and the selection of working point, thus enhancing the dynamic performance of self-compensation, which makes it possible for a SERF inertial measurement system to be used in complex magnetic field environments.

Author Contributions: Conceptualization, L.Y. and H.P.; methodology, L.Y.; software, L.Y.; validation, L.Y., H.P. and W.Q.; formal analysis, L.Y.; investigation, H.P.; resources, H.P.; data curation, L.Y.; writing—original draft preparation, L.Y.; writing—review and editing, H.P. and W.Q.; visualization, L.Y.; supervision, H.P.; project administration, W.Q.; funding acquisition, H.P. and W.Q. All authors have read and agreed to the published version of the manuscript.

Funding: This work was supported by the National Science Fund for Distinguished Young Scholars China (61925301) and China Postdoctoral Science Foundation (Grant No. 2023M730181).

Institutional Review Board Statement: Not applicable.

Informed Consent Statement: Not applicable.

Data Availability Statement: Data underlying the results presented in this paper are not publicly available at this time but may be obtained from the authors upon reasonable request.

Conflicts of Interest: The authors declare no conflict of interest.

References

1. Budker, D.; Romalis, M. Optical magnetometry. *Nat. Phys.* **2007**, *3*, 227–234. [CrossRef]
2. Fang, J.; Wan, S.; Yuan, H. Dynamics of an all-optical atomic spin gyroscope. *Appl. Opt.* **2013**, *52*, 7220–7227. [CrossRef]
3. Limes, M.; Sheng, D.; Romalis, M.V. He 3–Xe 129 comagnetometery using Rb 87 detection and decoupling. *Phys. Rev. Lett.* **2018**, *120*, 033401. [CrossRef]
4. Liu, S.; Wang, Z.; Zhai, Y. In-Situ Detection for Atomic Density in the K-Rb-21Ne Co-Magnetometer via an Optical Heterodyne Interferometry. *Photonics* **2023**, *10*, 1091. [CrossRef]
5. Boto, E.; Holmes, N.; Leggett, J.; Roberts, G.; Shah, V.; Meyer, S.S.; Muñoz, L.D.; Mullinger, K.J.; Tierney, T.M.; Bestmann, S.; et al. Moving magnetoencephalography towards real-world applications with a wearable system. *Nature* **2018**, *555*, 657–661. [CrossRef]
6. Allmendinger, F.; Schmidt, U.; Heil, W.; Karpuk, S.; Scharth, A.; Sobolev, Y.; Tullney, K.; Zimmer, S. New limit on Lorentz and CPT violating neutron spin interactions using a free precession 3He-129Xe co-magnetometer. *Phys. Rev. Lett.* **2014**, *85*, 110801. [CrossRef]
7. Bear, D.; Stoner, R.; Walsworth, R.; Kostelecký, V.A.; Lane, C.D. Limit on Lorentz and CPT violation of the neutron using a two-species noble-gas maser. *Phys. Rev. Lett.* **2000**, *85*, 5038. [CrossRef]
8. Ledbetter, M.; Savukov, I.; Romalis, M. Nonlinear amplification of small spin precession using long-range dipolar interactions. *Phys. Rev. Lett.* **2005**, *94*, 060801. [CrossRef] [PubMed]
9. Vasilakis, G.; Brown, J.; Kornack, T.; Romalis, M. Limits on new long range nuclear spin-dependent forces set with a K- He 3 comagnetometer. *Phys. Rev. Lett.* **2009**, *103*, 261801. [CrossRef] [PubMed]
10. Wei, K.; Ji, W.; Fu, C.; Wickenbrock, A.; Flambaum, V.V.; Fang, J.; Budker, D. Constraints on exotic spin-velocity-dependent interactions. *Nat. Commun.* **2022**, *13*, 7387. [CrossRef] [PubMed]
11. Walker, T.G.; Happer, W. Spin-exchange optical pumping of noble-gas nuclei. *Rev. Mod. Phys.* **1997**, *69*, 629. [CrossRef]
12. Kornack, T.; Romalis, M. Dynamics of two overlapping spin ensembles interacting by spin exchange. *Phys. Rev. Lett.* **2002**, *89*, 253002. [CrossRef] [PubMed]
13. Zhao, T.; Liu, Y.; Wei, K.; Xie, H.; Mu, T.; Fang, X.; Xu, Z.; Zhai, Y. Ultra-sensitive all-optical comagnetometer with laser heating. *J. Phys. D Appl. Phys.* **2022**, *55*, 165103. [CrossRef]
14. Wei, K.; Zhao, T.; Fang, X.; Xu, Z.; Liu, C.; Cao, Q.; Wickenbrock, A.; Hu, Y.; Ji, W.; Fang, J.; et al. Ultrasensitive atomic comagnetometer with enhanced nuclear spin coherence. *Phys. Rev. Lett.* **2023**, *130*, 063201. [CrossRef] [PubMed]
15. Xu, Z.; Wei, K.; Zhao, T.; Cao, Q.; Liu, Y.; Hu, D.; Zhai, Y. Fast dynamic frequency response-based multiparameter measurement in spin-exchange relaxation-free comagnetometers. *IEEE Trans. Instrum. Meas.* **2021**, *70*, 1–10. [CrossRef]
16. Kornack, T.; Ghosh, R.; Romalis, M.V. Nuclear spin gyroscope based on an atomic comagnetometer. *Phys. Rev. Lett.* **2005**, *95*, 230801. [CrossRef]
17. Fang, J.; Qin, J. Advances in atomic gyroscopes: A view from inertial navigation applications. *Sensors* **2012**, *12*, 6331–6346. [CrossRef]
18. Shi, M. Investigation on magnetic field response of a 87 Rb-129 Xe atomic spin comagnetometer. *Opt. Express* **2020**, *28*, 32033–32041. [CrossRef]
19. Babcock, E.; Nelson, I.; Kadlecek, S.; Driehuys, B.; Anderson, L.; Hersman, F.W.; Walker, T.G. Hybrid Spin-Exchange Optical Pumping of He 3. *Phys. Rev. Lett.* **2003**, *91*, 123003. [CrossRef] [PubMed]
20. Smiciklas, M.; Brown, J.; Cheuk, L.; Smullin, S.; Romalis, M.V. New Test of Local Lorentz Invariance Using a Ne 21-Rb-K Comagnetometer. *Phys. Rev. Lett.* **2011**, *107*, 171604. [CrossRef] [PubMed]
21. Fang, J.; Chen, Y.; Zou, S.; Liu, X.; Hu, Z.; Quan, W.; Yuan, H.; Ding, M. Low frequency magnetic field suppression in an atomic spin co-magnetometer with a large electron magnetic field. *J. Phys. At. Mol. Opt. Phys.* **2016**, *49*, 065006. [CrossRef]
22. Li, Y.; Liu, X.J.; Cai, H.W.; Ding, M.; Fang, J.C. Optimization of the alkali-metal density ratio in a hybrid optical pumping atomic magnetometer. *Meas. Sci. Technol.* **2018**, *30*, 015005. [CrossRef]
23. Lancor, B.; Walker, T.G. Polarization limits in K-Rb spin-exchange mixtures. *Phys. Rev. A* **2011**, *83*, 065401. [CrossRef]
24. Wei, K.; Zhao, T.; Fang, X.; Li, H.; Zhai, Y.; Han, B.; Quan, W. Simultaneous Determination of the Spin Polarizations of Noble-Gas and Alkali-Metal Atoms Based on the Dynamics of the Spin Ensembles. *Phys. Rev. Appl.* **2020**, *13*, 044027. [CrossRef]
25. Tang, J.; Yin, Y.; Zhai, Y.; Zhou, B.; Han, B.; Yang, H.; Liu, G. Transient dynamics of atomic spin in the spin-exchange-relaxation-free regime. *Opt. Express* **2021**, *29*, 8333–8343. [CrossRef]
26. Ghosh, R.K.; Romalis, M.V. Measurement of spin-exchange and relaxation parameters for polarizing ^{21}Ne with K and Rb. *Phys. Rev. A* **2010**, *81*, 043415. [CrossRef]

27. Stone, N. Table of nuclear magnetic dipole and electric quadrupole moments. *At. Data Nucl. Data Tables* **2005**, *90*, 75–176. [CrossRef]
28. Yang, L.; Pang, H.; Wei, Y.; Quan, W. Optimizing noble gas pressure for enhanced self-compensation in spin-exchange relaxation-free comagnetometers. *Opt. Express* **2023**, *31*, 33274–33286. [CrossRef]
29. Brown, J.; Smullin, S.; Kornack, T.; Romalis, M. New limit on lorentz-and C P T-violating neutron spin interactions. *Phys. Rev. Lett.* **2010**, *105*, 151604. [CrossRef]
30. Ruan, J.; Duan, L.; Fu, Y.; Fan, W.; Quan, W. Effects of pump laser intensity on the cell temperature working point in a K-Rb-21 Ne spin-exchange relaxation-free co-magnetometer. *Opt. Express* **2023**, *31*, 8342–8351. [CrossRef]